PCCP

Accepted Manuscript

This is an *Accepted Manuscript*, which has been through the Royal Society of Chemistry peer review process and has been accepted for publication.

Accepted Manuscripts are published online shortly after acceptance, before technical editing, formatting and proof reading. Using this free service, authors can make their results available to the community, in citable form, before we publish the edited article. We will replace this *Accepted Manuscript* with the edited and formatted *Advance Article* as soon as it is available.

You can find more information about *Accepted Manuscripts* in the Information for Authors.

Please note that technical editing may introduce minor changes to the text and/or graphics, which may alter content. The journal's standard Terms & Conditions and the Ethical guidelines still apply. In no event shall the Royal Society of Chemistry be held responsible for any errors or omissions in this *Accepted Manuscript* or any consequences arising from the use of any information it contains.

ROYAL SOCIETY OF CHEMISTRY

www.rsc.org/pccp

PCCP

Paper

Self-Powered Broadband, High-Detectivity and Ultrafast Photodetectors Based on Pd-MoS_2/Si Heterojunctions

Received 00th September 2015,
Accepted 00th January 2015

DOI: 10.1039/x0xx00000x

www.rsc.org/PCCP

L. Z. Hao,*[a,b] W. Gao,[b] Y. J. Liu,[b] Y. M. Liu,[b] Z. D. Han,[b] Q. Z. Xue*[a] and J. Zhu[c]

In this work, a self-powered photodetector device is fabricated through the integration of the palladium-doped molybdenum disulfide thin film on silicon (Pd-MoS_2/Si). The substitution of host Mo atoms with the Pd dopants in the MoS_2 film is revealed by structural and chemical analysis techniques. Due to the incorporation of Pd atoms into the MoS_2 films, the photovoltaic characteristics of the fabricated Pd-MoS_2/Si device were enhanced largely, promoting its applications as self-powered photodetectors operated at zero bias voltage. The obtained results further shows that the device is highly sensitive to broadband wavelength from the ultraviolet to near-infrared light (300-1100 nm). Especially, the Pd-MoS_2/Si photodetector shows an ultra-high detectivity of ~10^{14} Jones (Jones=cmHz$^{1/2}$W^{-1}), a responsivity of ~654.0 mAW^{-1}, and an ultrafast response speed of ~2.1 μs. The present work opens new avenues for developing high-performance photodetectors for optical communications and imaging techniques as well as optoelectronic circuits.

Introduction

Due to the low energy consumption, safe operation and simplifying design of driving circuits, self-powered photodetectors based on Schottky junctions or *p-n* junctions have attracted much attention in many fields, such as optical communications and imaging.[1] These photodetectors are driven by the built-in electrical field at the junction interface and they can work under zero bias voltage due to their photovoltaic behaviors. To date, great progress has been made in fabricating self-powered photodetectors. Various kinds of nanostructures have been applied in this area, such as CdSe nanobelts, TiO_2 films, CdS nanoribbon, and ZnO nanorods.[2] However, the results from these devices show that the range of detectable light wavelengths is generally limited in the narrow range of the ultraviolet or the visible lights, the detectivity is very low (10^7-10^{10} Jones) (Jones= cmHz$^{1/2}$W^{-1}), and the response speed is relatively slow (60-300 μs). It is therefore still a significant challenge to fabricate simple nanoscale devices toward self-powered broadband detectors with high detectivity and fast response speeds under weak light conditions, which will promote remarkably their applications in future nano-optoelectronic integrated circuits.

Molybdenum disulfide (MoS_2) has become one of the hottest research topics due to its good electrical, mechanical, optical, magnetic and electrochemical properties.[3] As a typical kind of layered transition metal dichalcogenides, MoS_2 is a stack of planes where covalently bonded S-Mo-S atoms in layers are closely packed in a hexagonal arrangement. The adjacent planes are held together by van der Waals interactions. It is reported that MoS_2 shows one order of magnitude higher sunlight absorption than the most commonly used sunlight absorbers of Si and GaAs.[4] Thus, MoS_2-based materials have been used to develop various optoelectronic devices, such as photodetectors and solar cells.[5,6] Usually, junction-type configurations are constructed for MoS_2 as the active material in the practical optoelectronic device applications. Similar to traditional semiconductor technologies, stable *n*- and *p*-type conduction in the MoS_2 is indispensable in these devices. Native MoS_2 belongs an *n*-type semiconductor owing to the existence of the sulfur vacancies. The semiconductor characteristics of *n*-type MoS_2 can be modulated by several techniques, such as metal work-function engineering,[7] surface functionalization,[8] and charge transfer from the absorbed volatile molecules.[9] However, it is still difficult to obtain stable *p*-type doping in MoS_2 due to its native elections concentration, despite the suggestion that *p*-type operation is more desirable for MoS_2-based field-effect transistor devices.[10] The *p*-type MoS_2 was obtained via a plasma-assisted doping approach by Wi *et al.*,[11] while Suh *et al.* demonstrated the stable *p*-type conduction in MoS_2 by substitutional niobium doping.[12] By these techniques, homojunctions composed of vertically stacked MoS_2 monolayers were fabricated. However, these devices usually suffer poor optoelectronic performance. For example, a low power-conversion efficiencies (only ~2.8%) was resulted due to its weak absorption to light, and the narrow detectable wavelength range. Comparatively, the formation of heterojunctions by combining MoS_2 with other semiconductors supplies a feasible route to construct high-performance optoelectronic devices by harnessing the advantages of both materials. Presently, silicon (Si) is dominating the commercial electronic device market due to its high abundance and mature processing technology. In order to develop practically applicable

[a] State Key Laboratory of Heavy Oil Processing, China University of Petroleum, Qingdao, Shandong 266580, P. R. China. haolanzhong@upc.edu.cn; xueqz@upc.edu.cn
[b] College of Science, China University of Petroleum, Qingdao, Shandong 266580, China
[c] State Key Laboratory of Electronic Thin Films and Integrated Devices, University of Electronic Science and Technology of China, Chengdu 610054, P. R. China.
Electronic Supplementary Information (ESI) available: See

This journal is © The Royal Society of Chemistry 2015

Physical Chemistry Chemical Physics Accepted Manuscript

optoelectronic devices, it is of great valuable to realize the integration of MoS_2 on Si. It should be further addressed that MoS_2 are fully compatible with Si fabrication technology.[13] So far, extensive efforts have been devoted to MoS_2/Si optoelectronic devices. For example, Esmaeili-Rad et al. reported the fabrication of photodetectors composed of MoS_2 films and amorphous Si (a-Si).[14] Despite the high responsivity of 210 mAW^{-1}, the device exhibited a slow response speed of 0.3 ms due to a large quantities of the structural defects in a-Si, especially large external voltages are necessary to supply the work power for the device. To improve the photoelectrical properties of the devices, single-crystal Si (sc-Si) has been used as the substrate to grow MoS_2 thin layers and MoS_2/sc-Si *n-p* heterojunctions were realized by Tsai et al.[15] The device achieved a power conversion efficiency of 5.23%. Furthermore, using a MoS_2 thin film as an effective electron-blocking/hole-transporting layer, a high photovoltaic conversion efficiency of 11.1% was achieved in the graphene/MoS_2/Si solar cell.[16] This supplies the possibility for MoS_2/Si to work without any external bias voltage as a photodetector.

In this work, palladium-doped MoS_2 (Pd-MoS_2) thin films were deposited onto Si substrates using dc magnetron sputtering technique. The substitution of host Mo atoms with the Pd dopants in the MoS_2 film was confirmed by structural and chemical analysis techniques and the *p*-type nature of the film were resulted. Due to the substitutionally incorporation of Pd atoms into the MoS_2 films, a large enhancement of photovoltaic characteristics was achieved in the Pd-MoS_2/Si *p-n* junction device, enabling its applications as self-powered photodetectors operated at zero bias voltage. The MoS_2/Si photodetectors showed excellent properties in terms of wide detection range, as well as high detectivity and high responsivity, and ultrafast response speed.

Experimental section

Pd-MoS_2 thin films were deposited on (100)-oriented Si substrates using dc magnetron sputtering technique. The Pd powders and MoS_2 powders (purity, 99.9%) with the atomic ratio of 1:99 were firstly ball milled for 2 h and then the mixture was cold-pressed into disk as the target during sputtering under 20 MPa. The Si substrates used in this work are *n*-type semiconductors with the resistivity of 3.2-6.8 Ω cm. Before the deposition, the substrates were ultrasonically cleaned in sequence by alcohol, acetone, and de-ionized water. Then, the substrates were dipped into HF solution (~5.0%) for 60.0 s to remove the natural oxide layer from the Si surface. After that, oxidation treatment of the substrates were performed in peroxide solution (~40.0%) at 100 °C for 20.0 min to form a ~3.0-nm-thickness SiO_2 passivation layer on the Si surface. Subsequently, ~30-nm-thickness MoS_2 thin films were deposited. During the deposition, the working pressure of argon gas and deposition temperature were 5.0 Pa and 400.0 °C, respectively. Finally, the top ~40-nm-thickness Pd electrode layer was fabricated on the Pd-MoS_2 film using dc magnetron sputtering technique. The whole top surface of the film was covered by the electrode layer. The back ~500-nm-thickness indium (In) electrode was covered on the whole backside of the Si substrate using thermal evaporation. As a reference, pure MoS_2 films without Pd doping were also deposited under the same growth conditions.

Samples were characterized using Raman spectroscopy (Renishaw, 514 nm laser). X-ray diffraction (XRD) patterns of the sample were performed on a Bede D1 X-ray diffractometer with Cu-Kα radiation (λ=0.15406 nm). Surface morphologies were studied by atomic force microscope (AFM, SPM-300HV, SEIKO). X-ray photoemission spectroscopy (XPS) was performed by a Kratos Axis ULTRA spectrometer using a monochromatic Al Kα x-ray source (1486.6 eV). The transmission spectra were measured by Shimadzu UV-3150 spectrophotometer. Ultraviolet photoelectron spectroscopy (UPS) measurements were made using an unfiltered He-I (21.22 eV) gas discharge lamp. The *I-V* curves were measured using two-point measurement by a Keithley2400 source meter at RT. To obtain the sensitivity of the device, a Xe lamp with tuneable output power combined with double monochromators (7ISW302 and 7ISW304, Sofn Instruments Co., Ltd, China) was used to produce the monochromatic light from 200-2500 nm. The response speed of the photodetector was evaluated by combining a pulse laser of 980 nm (SCT-DSL, Shaanxi Scitower Photoelectricity Equipment Co., Ltd, China) and a digital oscilloscope (Tektronix TDS 2012C).

Results and discussion

Fig. 1a shows the Raman spectra of the as-grown MoS_2 film (bottom) and Pd-MoS_2 (top) film on Si substrates. As shown in the figure, the MoS_2 film exhibits two characteristic Raman peaks, the E^1_{2g} mode at ∼376 cm^{-1} and the A_{1g} mode at ∼410 cm^{-1}. These results are consistent with other reported results.[17] The E^1_{2g} mode corresponds to the S and Mo atoms oscillating in antiphase parallel to the crystal plane and the A_{1g} mode corresponds to the S atoms oscillating in antiphase out-of-plane, as shown in the insets. From the figure, obvious red shift of about 6.0 cm^{-1} of the A_{1g} peak can be observed due to the incorporation of Pd atoms in the film, while the position of the E^1_{2g} peak almost has no change. As a result, the separation (Δ) between the E^1_{2g} and A_{1g} peaks decreases from 34.0 cm^{-1} of the MoS_2 film to 28.0 cm^{-1} of the Pd-MoS_2 film. In MoS_2-based materials, A_{1g} phonons couple much more tightly with electrons than E^1_{2g} phonons.[8] Hence, this demonstrates that the significant change of the electronic structure and semiconductor characteristics of the film can be caused by the Pd doping. Additionally, both the separations are much larger than those for the reported monolayer and several-layer MoS_2.[18] Fig. 1b shows the XRD pattern of the MoS_2 thin films. All the diffraction peaks can be indexed to MoS_2 with a hexagonal phase. Obvious diffraction peaks of the film at 33.9° and 69.1° corresponding to (100) and (200) can be observed from the figure. This demonstrates that the deposited MoS_2 film on the Si substrate in our work has the preferential [100] orientation. In other words, S-Mo-S unite layers in the film are aligned perpendicular to the substrate. This is completely different with the results for the monolayer MoS_2 prepared by the conventional chemical vapour deposition method. According to other reports,[19] the monolayer MoS_2 are usually lying on the substrate with (001) planes parallel to the substrate surface. The unique vertically-standing structure would open up exciting opportunities for various electronic and optoelectronic devices, complementary to the recent MoS_2-based devices with horizontal atomic layers. Fig. 1c shows AFM topographic image of the Pd-MoS_2

Physical Chemistry Chemical Physics Accepted Manuscript

This journal is © The Royal Society of Chemistry 2015

thin film grown on the Si substrate. As shown in the figure, the rough surface is evident. According to the measurements, the root-mean-square roughness (RMS) of the film is about 1.1 nm, and the average size of grains is ~30.4 nm in diameter.

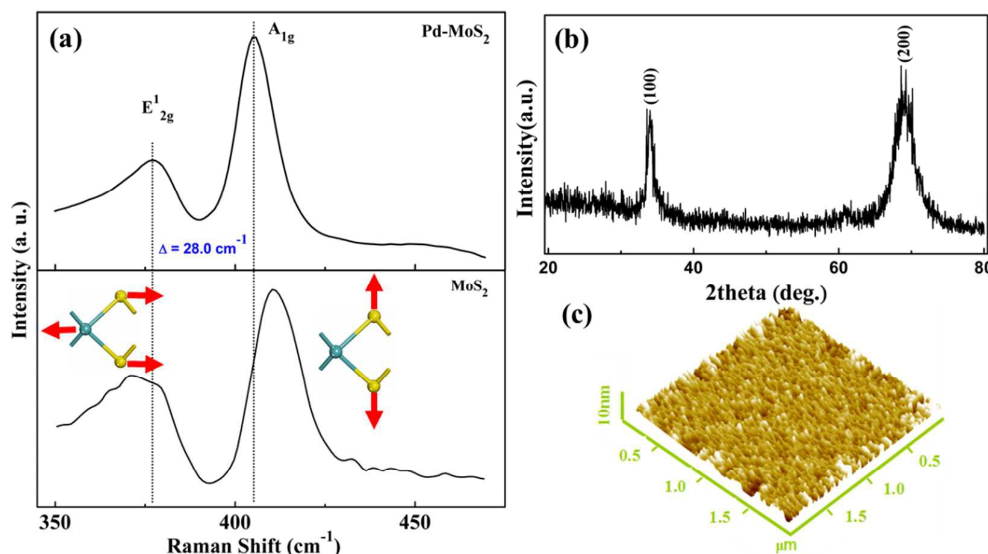

Fig. 1 (a) Raman spectra of Pd-MoS_2 film (top) and MoS_2 film (bottom). The insets show the schematic illustrations of the oscillating mode of E^1_{2g} (left) and A_{1g} (right), respectively. Atom color code: light blue-green, Mo; yellow, S. (b) XRD patterns of the Pd-MoS_2 film. (c) AFM surface morphology of the Pd-MoS_2 film on Si substrates.

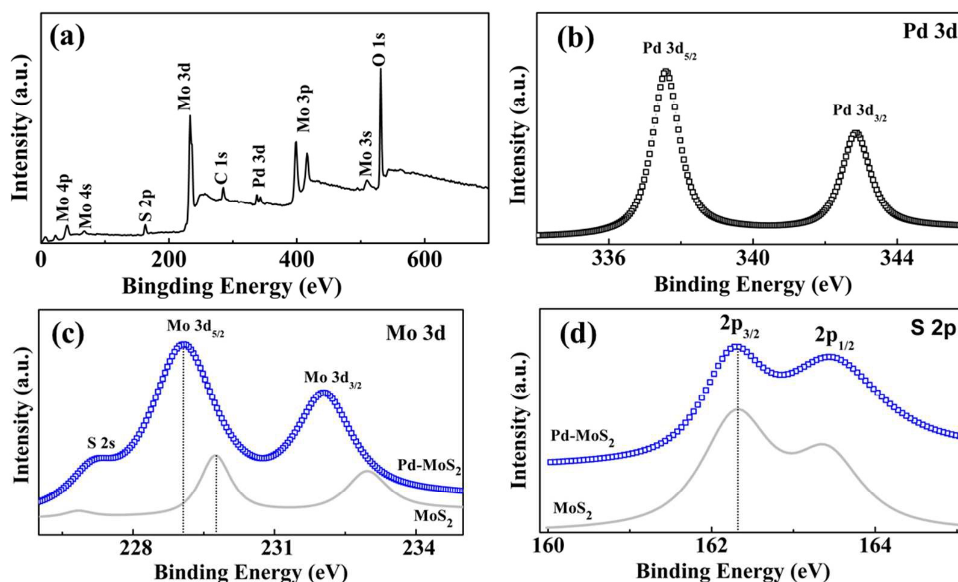

Fig. 2 (a) XPS spectrum of the Pd-MoS_2 film. (b), (c) and (d) Binding energies of Pd 3d, Mo 3d and S 2p for Pd-MoS_2 film. The light gray curves in (c) and (d) show comparatively the XPS binding energies of Mo and S for the MoS_2 film.

Fig. 2a shows the typical XPS spectrum of Pd-MoS_2 film, illustrating the presence of Pd, Mo and S coexisted in the film. Additionally, the existence of C and O elements can be observed from the spectrum. This might be caused by the absorbed gaseous molecules. Fig. 2b provides the binding energies of Pd elements in the Pd-MoS_2 film. Two peaks at 337.6 eV and 342.9 eV are assigned to Pd $3d_{5/2}$ and $3d_{3/2}$, respectively. The binding energies are much larger than those for Pd metals[20] and almost same with the characteristics of Pd^{4+}.[21] This reveals that the substitution of Mo atoms with Pd dopants is realized successfully and the Pd atoms are stabilized by covalent bonding inside the lattice. A typical high resolution XPS spectrum of Mo 3d and S 2p are shown in Figure 2c and d. The light gray curves show comparatively the binding energies of Mo and S for the MoS_2 film without Pd doping. The peaks at 229.1 and 232.1 eV are assigned to Mo $3d_{5/2}$ and Mo $3d_{3/2}$ orbital, respectively. As shown in the figure, the core-level peaks of Mo in the Pd-MoS_2 show a uniform shift toward lower binding energies compared to those of the undoped MoS_2 film. This shift

Physical Chemistry Chemical Physics Accepted Manuscript

can be attributed to the lowering of the Fermi level (E_F) upon the *p*-type doping, as similarly observed in previous studies.[22] According to the calculation, the amount of the shift of the binding energy is about 0.59 eV. The S $2p_{1/2}$ and S $2p_{3/2}$ appear at 163.5 and 162.2 eV, respectively, and there is almost no obvious difference of the binding energies between the films with and without Pd doping.

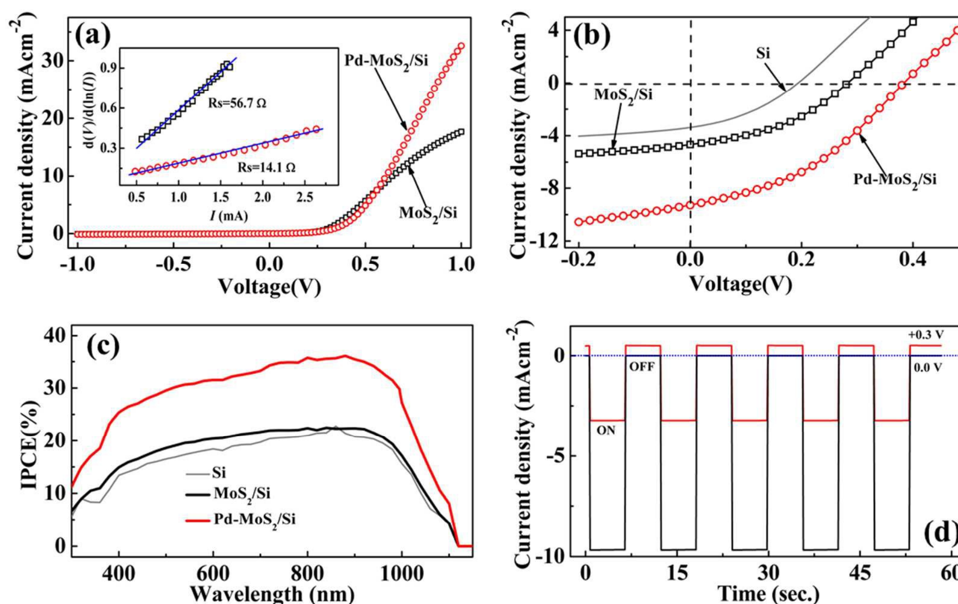

Fig. 3 (a) Dark *I-V* curves of the Pd-MoS_2/Si and MoS_2/Si devices, respectively. The inset shows the plot of d(*V*)/d(ln(*I*)) versus *I* for the above two devices in the forward voltage range. (b) Photovoltaic characteristics of three kinds of solar cells measured under 30.0 $mWcm^{-2}$, including Pd-MoS_2/Si, MoS_2/Si and Si. (c) Corresponding IPCE curves of the solar cells. The light gray curves in (b) and (c) show comparatively the referenced curves of the related properties for the Pd/Si Schottky-type device. (d) Photoresponse under zero bias and under a small forward bias when irradiation is turned on (5.0 s) and off (5.0 s), repeated for five cycles.

Fig. 3a shows the *I-V* characteristics of the MoS_2/Si and Pd-MoS_2/Si devices under the dark condition. Here, the forward voltages are defined as the positive voltages applied on the Pd top electrode. From the figure, obvious rectifying characteristics for both devices can be observed. The rectification ratio (I_+/I_-) at ±1.0 V reaches 10^2 order of magnitude for the devices. In our studies, both the Pd/MoS_2 and In/Si contacts are ohmic (ESI, Fig. S1†). Thus, the rectifying characteristics in the device can be mainly attributed to the Pd-MoS_2 (MoS_2)/Si junction. Compared to the MoS_2/Si, the Pd-MoS_2/Si device shows a large increase of the current in the forward voltage range. The series resistance (R_s) of the devices can be deduced from the slope of the d(*V*)/d(ln(*I*)) versus *I* plot in a large *I* region.[23] According to the fitted results, the R_s decreases from 56.7 Ω for the MoS_2/Si to 14.1 Ω for the Pd-MoS_2/Si, as shown in the inset. The enhancement of the conduction of the Pd-MoS_2 film along the out-of-plane orientation might be the only reason for the decrease of the series resistance. It demonstrates that the transportation of carriers in the film can be greatly facilitated by the Pd doping. This is also helpful to the transportation of the photoexcited carriers in the film, enhancing the photosensitivity of the device. The *I-V* curves of the devices under 30.0 $mWcm^{-2}$ white-light illumination are shown in Fig. 3b. Obvious photovoltaic characteristics for all the devices can be observed. According to our measurements, the MoS_2/Si device has a short circuit current density (J_{sc}) of 4.7 mA, an open circuit voltage (V_{oc}) of 0.28 V and a power conversion efficiency (PCE) of 1.7%. When the Pd atoms are incorporated into the MoS_2 film, the photovoltaic characteristics are enhanced largely, as shown in the figure. For the Pd-MoS_2/Si solar cell, V_{OC} and J_{SC} of the device increases to 0.39 V and 9.3 $mAcm^{-2}$, respectively. The overall PCE reaches 4.6%, up to a six-fold increase compared to the referenced device. These excellent photovoltaic properties can promise the applications of the Pd-MoS_2/Si device as self-powered photodetectors operated at zero bias voltage. Fig. 3c shows the corresponding incident photon-to-electron conversion efficiency (IPCE) curves of the devices. As shown in the figure, the IPCE values of the Pd-MoS_2/Si device are much larger than those for the MoS_2/Si and Si solar cells over the full wavelength range, 300-1100 nm. This further demonstrates that the Pd-MoS_2/Si has higher efficiencies on carrier collection. Fig. 3d shows the photoresponse of the Pd-MoS_2/Si device under zero bias and a small forward bias (+0.3 V) under the light illumination. Five cycles of switching the light on and off show good stability and repeatability of the photoresponse of the device. When the light-on and light-off conditions are switched alternately, two distinct photovoltage states for the device are shown, the ''low'' state in dark and the ''high'' state in light. Both the steep rise and fall edges indicate that the photoexcited carriers can be separated rapidly. Moreover, the device shows a binary response under a smaller forward bias than V_{OC}. It is well known that the signal-noise ratio is the main factor to limit the accuracy of the photodetector under the relatively weak light signal. The binary response is an effective way to remove the negative effect of noise signal.[24] From the figure, the direction of the current at +0.3 V can be observed to alternate between positive and negative when the light is switched on and

This journal is © The Royal Society of Chemistry 2015

Physical Chemistry Chemical Physics Accepted Manuscript

off. This phenomenon offers the opportunity to use the device as an on-off binary response device for reliable and stable detection to weak light signals.

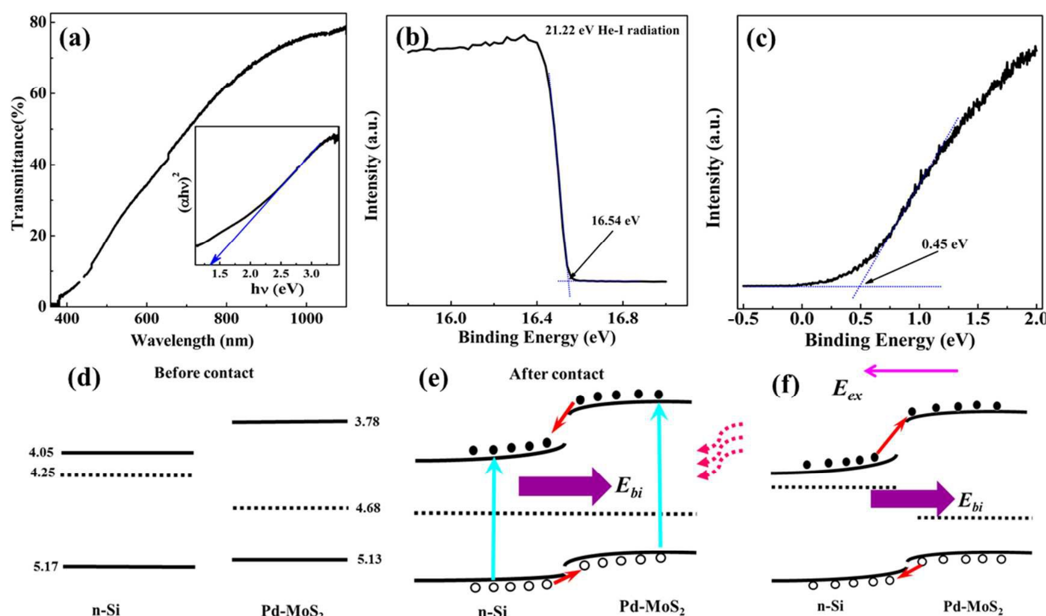

Fig. 4 (a) Transmission spectrum of the Pd-MoS_2 film deposited on glass substrate under the same growth condition with the film on Si. The inset shows a plot of $(\alpha h\nu)^2$ versus $h\nu$ for the Pd-MoS_2. (b) and (c) UPS spectra of the Pd-MoS_2 film on Si, showing the Fermi level of the Pd-MoS_2 film and the distance between the Fermi level and the conduction band, respectively. (d) and (e) are the energy band diagram before and after contact Pd-MoS_2/Si devices, respectively. (f) Energy band diagram of the Pd-MoS_2/Si devices under a small positive bias.

Fig. 4a shows the transmission spectrum of the Pd-MoS_2 film deposited on glass (a-SiO_2) substrate using the same growth condition with that on Si. As shown in the figure, the transmittance of the film decreases with decreasing the wavelength from near-infrared region to ultraviolet region (1100-300nm). Using the data from the transmittance spectrum, $(\alpha h\nu)^2$ is plotted as a function of photon energy $h\nu$, wherein h is the Planck constant and ν is photon frequency. The α is the absorption coefficient, calculated by $\alpha d=\ln(1/T)$, d and T are thickness and transmittance of the film, respectively.[25] The band gap (E_g) of the film can be determined by the intercept of the line on $h\nu$ axis, E_g=1.35 eV. The energy-band value for the film is a little larger than MoS_2 bulk (~1.2 eV) and much smaller than the monolayer (~1.9 eV). Fig. 4b shows the UPS spectrum of the MoS_2 film on the Si substrate. The work function (W) of the film can be calculated from the difference between the cutoff of the highest binding energy and the photon energy of the exciting radiation. From the figure, W=4.68 eV can be obtained. Since the Fermi level (E_F) of MoS_2 exists between the conduction band (E_C) and the valence band (E_V), the distance (ΔE) between E_V and E_F of MoS_2 film can be extracted from the onset energy, as shown in Fig. 4c. The ΔE for Pd-MoS_2 is determined to be 0.45 eV. According to these energy-band parameters, the p-type behavior of the Pd-MoS_2 film can be proved, while the as-deposited MoS_2 film without Pd doping shows the n-type nature determined by UPS analysis (ESI, Fig. S2†). According to Periodic Table of Elements, the electronegativity of Pd is 2.20 while 2.16 for Mo. The p-type nature of the Pd-MoS_2 film might be caused by the stronger electronegativity of Pd than Mo. The larger electronegativity of the Pd atoms makes it more difficult for S to receive the electrons from Pd. This can cause large quantities of vacancies in the MoS_2 film and the native electron carriers can be compensated. As a result, p-type characteristics are exhibited in the Pd-MoS_2 films. The Fermi level of n-type Si is 4.21 eV, and its electron affinity (χ) and band gap are respectively 4.05 eV and 1.12 eV.[26] Based on the above results, the isolated energy-band diagrams of the Pd-MoS_2/Si are constructed, as shown in Fig. 4d. When the Pd-MoS_2 film is deposited onto the Si substrate, the electrons flow from Si into Pd-MoS_2 at the interface due to the lower Fermi energy level of the Pd-MoS_2. The flowing process stops when Fermi levels are equal and a Pd-MoS_2/Si p-n junction is fabricated, as shown in Fig. 4e. Consequently, a built-in electrical field (E_{bi}) is formed near the interface and its direction points from the substrate to the film. Under the light illumination, the incident photons generate the electron-hole (e-h) pairs in the Pd-MoS_2 film and the Si. The built-in electric field can effectively facilitate the separation of photo-generated e-h pairs, transporting separated electrons from Pd-MoS_2 to Si and holes towards Si. The processes of photo-excitation and carrier transport in the Pd-MoS_2/Si p-n junction are demonstrated in the figure. Therefore, obvious photovoltaic characteristics are resulted in the p-n junction. As is well known that the V_{OC} depends on the build-in field near the interface.[27] Due to the Pd doping in the MoS_2 film, the E_{bi} near the interface can be enhanced with the shift of the Fermi level of the film towards the E_V. Thus, the Pd-MoS_2/Si device shows a larger V_{OC} of 0.39 V compared to the device without the Pd doping. This photovoltaic effect enables the device to sense the light illumination without any external energy supply. As shown in Figure

Physical Chemistry Chemical Physics Accepted Manuscript

4d, when a small forward electrical field (E_{ex}) is applied on the device, a positive current in the circuit can be caused under the dark condition. However, under the light illumination, the photoinduced electromotive force is in the reverse direction to the E_{ex}. Therefore, an on-off binary response with the current change from positive to negative can be observed from Fig. 3d.

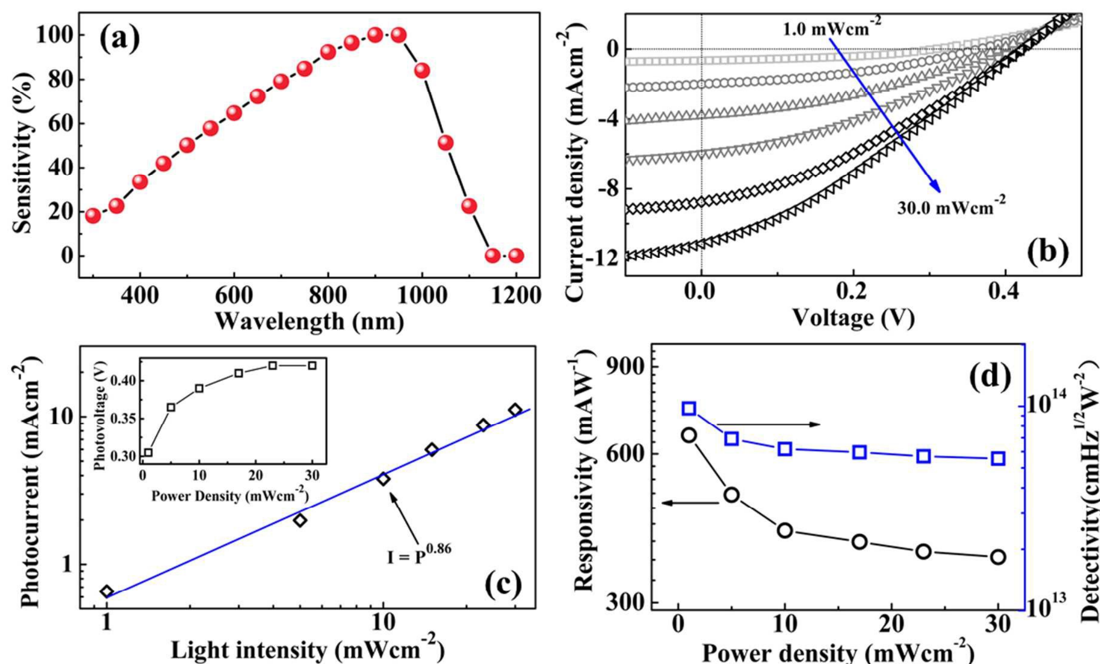

Fig. 5 (a) Sensitivity of the Pd-MoS_2/Si photodetector as a function of wavelength. (b) Photoresponse characteristics of the devices under 950 nm laser illumination with different light intensities. (c) Photocurent at zero external bias as a function of light intensity. The inset shows the photovoltage of the device as a function of light intensity. (d) Plot of the responsivity and detectivity as a function of the power density.

Fig. 5a shows the sensitivity of the Pd-MoS_2/Si photodetector as a function of wavelength. The sensitivity is defined as the value of I_p/I_d, where I_p and I_d represent the photocurrent and dark current, respectively. Here the normalization of the sensitivity of the device is used. From the figure, obvious photoresponse can be observed in a wide wavelength range from the ultraviolet to near-infrared area (300-1100 nm). The highest sensitivity of the device is located at around 950 nm and the real sensitivity reaches 3.1×10^5. The photon energy from 950-nm-wavelength light is consistent with the band gap of the Pd-MoS_2 film from the UPS results in Fig. 4a. This well demonstrates that the photoresponse of the device is dominated mainly by the Pd-MoS_2 film. Fig. 5b shows the *I-V* characteristics of the devices under 980 nm laser illumination with different light intensities from 1.0 mWcm^{-2} to 30.0 mWcm^{-2}. From the figure, we can see that both the photocurrent and photovoltage have a strong dependence on the incident light intensity and increase with the increasing light intensity. Fig. 5c shows the photocurent of the Pd-MoS_2/Si at zero bias as a function of light intensity. The dependency curve can be well fitted with a power law:[28]

$$I_p \propto P^{\theta} \quad (1)$$

In Eq. (1), I_p is the photocurrent, ϑ is the proportionality constant and P represent the light intensity. ϑ=0.86 can be obtained from the linear fitting. This value is close to the theoretical value of 1.0, implying the low trap density in the film.[29] The inset shows that the photovoltage of the device increases rapidly from 0.31 V to 0.42 V when the light intensity changes from 1.0 to 20.0 mW cm^{-2}. However, further increase of the light intensity leads to the saturation of the photovoltage. To evaluate the detection performance of the Pd-MoS_2/Si photodetector, the photoresponsivity (R) and the photodetectivity (D^*) are further calculated. The photoresponsivity can be described using the following equation:[30]

$$R = I_p / P_{in} \quad (2)$$

In Eq. (2), the I_p and P_{in} are the photocurrent and incidence light power, respectively. The high value of R mean that the high photocurrent generated per unit power of the incident light on the effecttive area. D^* is an important factor that reflects the ability of detecting a weak light signal from the noise environment. D^* can be calculated from the following expression:[31]

$$D^* = R / (2qJ_d)^{1/2} \quad (3)$$

In Eq. (3), J_d is the dark current density (only ~3.0×10^{-5} mAcm^{-2} in this work). Eq. (3) suggests that the D^* is determined by the dark current and the photoresponsivity to a large extent. Fig. 5d shows the R and D^* of the MoS_2/Si heterojunction under zero bias voltage as a function of incident light intensity. According to the calculated results, a high photoresponsivity and detectivity of about 371.0 mAW^{-1} and 5.6×10^{13} Jones can be obtained under the light intensity of 30.0 mWcm^{-2}. This is one order of magnitude larger than other results about the MoS_2-based photodetector.[32] As shown in the figure, both R and D^* increase with decreasing the power intensity.

This journal is © The Royal Society of Chemistry 2015
Physical Chemistry Chemical Physics Accepted Manuscript

Under a light intensity of 1.0 $mWcm^{-2}$, R increases to 654.0 mAW^{-1}, especially D^* reaches 1.0×10^{14} Jones which is much larger than the value for the commercially available Si photodetectors ($\leq10^{13}$ Jones).[33]

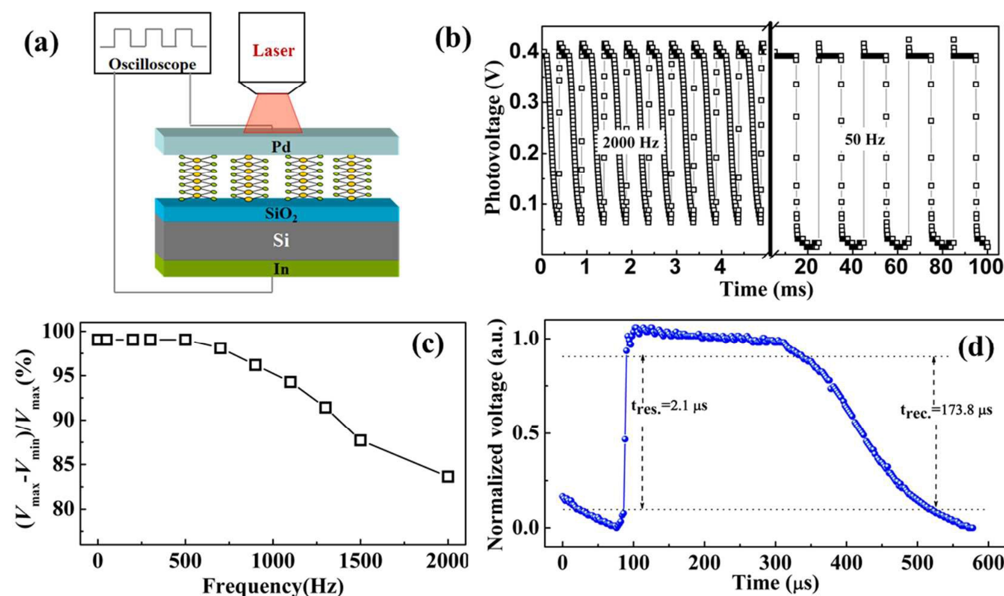

Fig. 6 (a) Schematic illustration of the setup for measuring the response time of the Pd-MoS_2/Si device. (b) Photoresponse of the photodetector to the pulsed light irradiation of 980 nm with a frequency of 50 Hz and 2000 Hz, respectively. (c) Relative balance versus switching frequency of the pulsed laser. (d) Single normalized modulation cycle measured at 2000 Hz.

Response speed for a photodetector is also crucial in practical applications. Fig. 6a shows the schematic illustration of the setup for measuring the response time of the Pd-MoS_2/Si device. The response and recovery time of the photodetector are measured using an oscilloscope and a 980-nm-wavelength pulsed laser source with the adjustable frequencies from 0 to 8000 Hz. The test was carried out under a zero applied field. Fig. 6b shows the photoresponse of the Pd-MoS_2/Si self-powered photodetector under the light switching frequencies of 2000 Hz and 50 Hz, respectively. As shown in the figure, the response is fast and shows excellent stability and repeatability. The relative balance of the photovoltage signals at different laser frequencies, $(V_{max}-V_{min})/V_{max}$, is calculated. Fig. 6c shows the plot of the relative balance versus laser frequency. As shown in the figure, the value of the relative balance only decreases by 15% when the laser frequency increase from 1 Hz to 2000 Hz, implying that the Pd-MoS_2/Si self-powered photodetector can work well in a wide switching frequency range. Fig. 6d shows the single normalized modulation cycle measured at 2000 Hz. The response time (t_{res}) is the time interval for the response to rise from 10% to 90% of its peak value. The recovery time (t_{rec}) is the time interval for the recovery to decay from 90% to 10% of its peak value. The device shows a fast response speed with t_{res}=2.1 μs. This value is among the best reported results for self-powered photodetectors.[2,5,32,34] Comparatively, longer time is exhausted for the recovery, t_{rec}=173.8 μs. The asymmetric relation between the response and recovery speeds is a familiar phenomenon for photodetectors due to the existence of the trap states in the film or near the interface.[35] The recovery speed would be improved great by further decreasing the defects in the film and at the interface.

The high performance of the fabricated Pd-MoS_2/Si photodetector could be mainly attributed to the incorporation of the Pd dopant in the MoS_2 film based on the following aspects: i) A strong build-in electrical field at the Pd-MoS_2/Si interface is formed due to the shift of the Fermi level caused by the Pd doping, which can greatly facilitate the separation of photo-generated carriers, leading to a high photo-induced current and high photoresponse in the device. ii) The transportation of the photoexcited carriers in the film can be facilitated by the Pd doping in the film and the high response speed can be obtained, as demonstrated in Fig. 3a and b. iii) Additionally, due to the high in-plane mobility of the MoS_2 layer, the unique vertically standing layered structure for the MoS_2 film could offer high-speed paths for the transportation of the photoexcited carriers along the out-of-plane orientation. This might be also responsible for the large photocurrent and high response speed.

Conclusion

In summary, Pd-MoS_2 thin films were deposited onto Si substrates using magnetron sputtering technique. The structural and chemical analysis show that the Pd dopants were incorporated into the film by the replace of host Mo atoms. This resulted in the *p*-type nature of the film. A Pd-MoS_2/Si photodetector was fabricated based on the *p-n* junction structure. Due to the incorporation of Pd atoms into the MoS_2 films, the photovoltaic characteristics of the Pd-MoS_2/Si device were enhanced greatly, enabling its applications as self-powered photodetectors. Under zero bias voltage, the Pd-MoS_2/Si device exhibited high photoresponse

Physical Chemistry Chemical Physics Accepted Manuscript

in a wide wavelength, from the ultraviolet to near-infrared light. Under the laser illumination of 980 nm, the Pd-MoS_2/Si photodetector shows an ultra-high detectivity of ~10^{14} Jones, a responsitivity of ~654.0 mAW^{-1}, and an ultrafast response speed of ~2.1 μs. These device performances are significantly better than those for commercially available photodetectors. The presented Pd-MoS_2/Si devices hold great promise in developing high-performance photodetectors.

Acknowledgements

The authors would like to acknowledge the financial support by the Fundamental Research Funds for the Central Universities (14CX05038A and 15CX08009A) and the National Science Foundation of China (Grant No. 51502348, 51102284 and 51372030).

Notes and References

1 L. Peng, L. Hu and X. Fang, *Adv. Funct. Mater.*, 2014, **24**, 2591.
2 T. Zhai, L. Li, X. Wang, X. Fang, Y. Bando and D. Golberg, *Adv. Funct. Mater*., 2010, **20**, 4233.
3 Y. Yoon, K. Ganapathi and S. Salahuddin, *Nano Lett.*, 2011, **11**, 3768; Q. Q. Ji, Y. F. Zhang, T. Gao, Y. Zhang, D. L. Ma, M. X. Liu, Y. B. Chen, X. F. Qiao, P. H. Tan, M. Kan, J. Feng, Q. Sun and Z. F. Liu, *Nano Lett.*, 2013, **13**, 3870; C. Ataca, H. Sahin, E. Aktuörk and S. Ciraci, *J. Phys. Chem. C*, 2011, **115**, 3934; J. Zhang, J. M. Soon, K. P. Loh, J. Yin, J. Ding, M. B. Sullivian and P. Wu, *Nano Lett.*, 2007, **7**, 2370; J. Chen, N. Kuriyama, H. Yuan, H. T. Takeshita and T. Sakai, *J. Am. Chem. Soc.*, 2001, **123**, 11813.
4 M. Bernardi, M. Palummo and J.C. Grossman, *Nano Lett.*, 2013, **13**, 3664.
5 X. Li, J. Wu, N. Mao, J. Zhang, Z. Lei, Z. Liu and H. Xu, *Carbon*, 2015, **92**, 126.
6 H. Xu, J. Wu, Q. Feng, N. Mao, C. Wang and J. Zhang, *Small*, 2014, **10**, 2300; M. Shanmugam, C. A. Durcan, B. Yu, *Nanoscale*, 2012, **4**, 7399; R. Cheng, D. Li, H. Zhou, C. Wang, A. Yin, S. Jiang, Y. Liu, Y. Chen, Y. Huang and X. Duan, *Nano Lett.*, 2014, **14**, 5590; L. Z. Hao, W. Gao, Y. J. Liu, Z. D. Han, Q. Z. Xue, W. Y. Guo, J. Zhu and Y. R. Li, *J. Appl. Phys.*, 2015, **117**, 114502; L. Z. Hao, W. Gao, Y. J. Liu, Z. D. Han, Q. Z. Xue, W. Y. Guo, J. Zhu and Y. R. Li, *Nanoscale*, 2015, **7**, 8304; W. Jie and J. Hao, *Nanoscale*, 2014, **6**, 6346.
7 S. Chuang, C. Battaglia, A. Azcatl, S. McDonnell, J. S. Kang, X. Yin, M. Tosun, R. Kapadia, H. Fang, R. M. Wallace and A. Javey, *Nano Lett.*, 2014, **14**, 1337.
8 J. D. Lin, C. Han, F. Wang, R. Wang, D. Xiang, S. Qin, X. Zhang, L. Wang, H. Zhang, A. T. S. Wee, W. Chen, *ACS Nano*, 2014, **8**, 5323.
9 S. Tongay, J. Zhou, C. Ataca, J. Liu, J. S. Kang, T. S. Matthews, L. You, J. Li, J. C. Grossman and J. Wu, Nano Lett., 2013, 13, 2831.
10 Y. J. Zhang, J. T. Ye, Y. Yomogida, T. Takenobu and Y. Iwasa, *Nano Lett.*, 2013, **13**, 3023.
11 S. Wi, H. Kim, M. Chen, H. Nam, L.J Guo, E. Meyhofer and X. Liang, *ACS Nano*, 2014, **8**, 5270.
12 J. Suh, T. E. Park, D. Y. Lin, D. Fu, J. Park, H. J. Jung, Y. Chen, C. Ko, C. Jang, Y. Sun, R. Sinclair, J. Chang, S. Tongay and J. Wu, *Nano Lett.*, 2014, **14**, 6976.
13 K. Lee, R. Gatensby, N. McEvoy, T. Hallam and G. S. Duesberg, *Adv. Mater.*, 2013, **25**, 6699.
14 M. R. Esmaeili-Rad and S. Salahuddin, *Scientific Rep.*, 2013, **3**, 2345.
15 M. L. Tsai, S. H. Su, J. K. Chang, D. S. Tsai, C. H. Chen, C. I. Wu, L. J. Li, L. J. Chen and J. H. He, *ACS Nano*, 2014, **8**, 8317.
16 Y. Tsuboi, F. Wang, D. Kozawa, K. Funahashi, S. Mouri, Y. Miyauchi, T. Takenobu and K Matsuda, *Nanoscale*, 2015, 7, 14476.
17 D. J. Late, P. A. Shaikh, R. Khare, R. V. Kashid, M. Chaudhary, M. A. More and S. B. Ogale, *ACS Appl. Mater. Interfaces*, 2014, **6**, 15881.
18 R. Ganatra and Q. Zhang, *ACS Nano*, 2014, **8**, 4074.
19 M. L. Tsai, S. H. Su, J. K. Chang, D. S. Tsai, C. H. Chen, C. I. Wu, L. J. Li, L. J. Chen and J. H. He, *ACS Nano*, 2014, **8**, 8317; Y. Shi, W. Zhou, A. Y. Lu, W. Fang, Y. H. Lee, A. L. Hsu, S. M. Kim, K. K. Kim, H. Y. Yang, L. J. Li, J. C. Idrobo and J. Kong, *Nano Lett.*, 2012, **12**, 2784.
20 L. Yuwen, F. Xu, B. Xue, Z. Luo, Q. Zhang, B. Bao, S. Su, L. Weng, W. Huang and L. Wang, *Nanoscale*, 2014, **6**, 5762.
21 J. Ye and C. Liu, *Chem. Commun*., 2011, **47**, 2167.
22 S. McDonnell, R. Addou, C. Buie, R. M. Wallace and C. L. Hinkle, *ACS Nano*, 2014, **8**, 2880.
23 W. Du, M. Baba, K. Toko, K. O. Hara, K. Watanabe, T. Sekiguchi, N. Usami and T. Suemasu, *J. Appl. Phys.*, 2014, **115**, 223701.
24 Q. Hong, Y. Cao, J. Xu, H. Lu, J. He and J. L. Sun, *ACS Appl. Mater. Interfaces*, 2014, **6**, 20887.
25 X. Chen, K. Ruan, G. Wu and D. Bao, *Appl. Phys. Lett.*, 2008, **93**, 112112.
26 K. Jiao, C. Duan, X. Wu, J. Chen, Y. Wang and Y. Chen, *Phys. Chem. Chem. Phys.*, 2015, **17**, 8182.
27 J. Shewchun, J. Dubow, A. Myszkowski and R. Singh, *J. Appl. Phys.*, 1978, **49**, 855.
28 L. H. Zeng, M. Z. Wang, H. Hu, B. Nie, Y. Q. Yu, C. Y. Wu, L. Wang, J. G. Hu, C. Xie, F. X. Liang and L. B. Luo, *ACS Appl. Mater. Interfaces*, 2013, **5**, 9362.
29 L. Li, E. Auer, M. Liao, X. Fang, T. Zhai, U.K. Gautam, A. Lugstein, Y. Koide, Y. Bando and D. Golberg, *Nanoscale*, 2011, **3**, 1120.
30 W. Choi, M. Y. Cho, A. Konar, J. H. Lee, G. B. Cha, S. C. Hong, S. Kim, J. Kim, D. Jena and J. Joo, *Adv. Mater.*, 2012, **24**, 5832.
31 M. S. Choi, D. Qu, D. Lee, X. Liu, K. Watanabe, T. Taniguchi, W. J. Yoo, *ACS Nano*, 2014, **8**, 9332.
32 L. Wang, J. Jie, Z. Shao, Q. Zhang, X. Zhang, Y. Wang, Z. Sun and S.T. Lee, *Adv. Func. Mater.*, 2015, **25**, 2910.
33 X. Gong, M. H. Tong, Y. J. Xia, W. Z. Cai, J. S. Moon, Y. Cao, G. Yu, C. L. Shieh, B. Nilsson and A. J. Heeger, *Science*, 2009, **325**, 1665.
34 J. Qi, X. Hu, Z. Wang, X. Li, W. Liu and Y. Zhang, *Nanoscale*, 2014, **6**, 6025; P. Lin, X. Yan, Y. Liu, P. Li, S. Lu and Y. Zhang, *Phys. Chem. Chem. Phys.*, 2014, **16**, 26697.
35 K. Liu, M. Sakurai, M. Aono and D. Shen, *Adv. Funct. Mater.*, 2015, **25**, 3157

Physical Chemistry Chemical Physics Accepted Manuscript

 This journal is © The Royal Society of Chemistry 2015